Bioink Temperature Influence on Shear Stress, Pressure and Velocity Using Computational Simulation

Authors:

J. Carlos Gómez-Blanco, Enrique Mancha-Sánchez, Alfonso C. Marcos, Manuel Matamoros, Antonio Díaz-Parralejo, J. Blas Pagador

Date Submitted: 2020-11-09

Keywords: Fluid Dynamics, temperature, level-set, commercial bioink, bioprinting material, computational simulation, bioprinting

Abstract:

Bioinks are usually cell-laden hydrogels widely studied in bioprinting performing experimental tests to tune their rheological properties, thus increasing research time and development costs. Computational Fluids Dynamics (CFD) is a powerful tool that can minimize iterations and costs simulating the material behavior using parametric changes in rheological properties under testing. Additionally, most bioinks have specific functionalities and their properties might widely change with temperature. Therefore, commercial bioinks are an excellent way to standardize bioprinting process, but they are not analyzed in detail. Therefore, the objective of this work is to study how three temperatures of the Cellink Bioink influence shear stress pressure and velocity through computational simulation. A comparison of three conical nozzles (20, 22, and 25G) for each temperature has been performed. The results show that shear stress, pressure, and velocity vary in negligible ranges for all combinations. Although these ranges are small and define a good thermo-responsive bioink, they do not generate a filament on the air and make drops during extrusion. In conclusion, this bioink provides a very stable behavior with low shear stress, but other bioprinting parameters must be set up to get a stable filament width.

Record Type: Published Article

Submitted To: LAPSE (Living Archive for Process Systems Engineering)

Citation (overall record, always the latest version):	LAPSE:2020.1135
Citation (this specific file, latest version):	LAPSE:2020.1135-1
Citation (this specific file, this version):	LAPSE:2020.1135-1v1

DOI of Published Version: https://doi.org/10.3390/pr8070865

processes

MDPI

Article

Bioink Temperature Influence on Shear Stress, Pressure and Velocity Using Computational Simulation

J. Carlos Gómez-Blanco [1,*], Enrique Mancha-Sánchez [1], Alfonso C. Marcos [2], Manuel Matamoros [2], Antonio Díaz-Parralejo [3] and J. Blas Pagador [1,*]

1 Jesús Usón Minimally Invasive Surgery Centre, 10002 Cáceres, Spain; emancha@ccmijesususon.com
2 Graphic Expression Department, Industrial Engineering School, Universidad de Extremadura, 06006 Badajoz, Spain; acmarcos@unex.es (A.C.M.); manuelmp@unex.es (M.M.)
3 Mechanical, Energy and Materials Engineering Department, Industrial Engineering School, Universidad de Extremadura, 06006 Badajoz, Spain; adp@unex.es
* Correspondence: jcgomez@ccmijesususon.com (J.C.G.-B.); jbpagador@ccmijesususon.com (J.B.P.)

Received: 28 May 2020; Accepted: 16 July 2020; Published: 17 July 2020

Abstract: Bioinks are usually cell-laden hydrogels widely studied in bioprinting performing experimental tests to tune their rheological properties, thus increasing research time and development costs. Computational Fluids Dynamics (CFD) is a powerful tool that can minimize iterations and costs simulating the material behavior using parametric changes in rheological properties under testing. Additionally, most bioinks have specific functionalities and their properties might widely change with temperature. Therefore, commercial bioinks are an excellent way to standardize bioprinting process, but they are not analyzed in detail. Therefore, the objective of this work is to study how three temperatures of the Cellink Bioink influence shear stress pressure and velocity through computational simulation. A comparison of three conical nozzles (20, 22, and 25G) for each temperature has been performed. The results show that shear stress, pressure, and velocity vary in negligible ranges for all combinations. Although these ranges are small and define a good thermo-responsive bioink, they do not generate a filament on the air and make drops during extrusion. In conclusion, this bioink provides a very stable behavior with low shear stress, but other bioprinting parameters must be set up to get a stable filament width.

Keywords: bioprinting; computational simulation; bioprinting material; commercial bioink; temperature; level-set; fluid dynamics

1. Introduction

Additive manufacturing technology is currently contributing with many possibilities to tissue engineering. In this sense, 2D structures created by standard procedures of tissue engineering can evolve into complex 3D structures using bioprinting [1]. Specifically, bioprinting could produce these complex structures by superposing biomaterial layers with several biological compounds that finally can generate artificial tissues and organs [2]. Bioprinting can also minimize rejection risk when patient's cells are used in the creation of autologous tissues and/or organs [1]. Bioprinting is usually divided into four main technologies: micro-extrusion, inkjet, laser-assisted, and stereolithography [3]. However, properties such as versatility, printing speed, and the possibility of using high viscous materials with a high cell density make micro-extrusion the most used bioprinting technique [1,3,4].

Because of their high importance in the bioprinting process, several studies analyzed how different materials affect cellular survival [5,6], printability [7–9], curing or cross-linking [9–12], and shape fidelity [13,14]. The bioinks used in bioprinting are usually cell-laden hydrogels with

very specific rheological properties. One of the most important properties is viscosity, which has a great impact on the bioink behavior of the bioink during bioprinting [15,16]. Most hydrogels are classified as non-Newtonian fluids, so their viscosity changes when a force is applied. Attending to this viscous behavior, non-Newtonian fluids are mainly classified into shear thickening (viscosity rises when shear rate increases) or shear thinning (viscosity decreases when shear rate increases). Some reviews focus their interest on these hydrogel properties and their influence on the bioprinting process [17–19]. Specifically, the material concentration was experimentally tested to analyze the behavior of the hydrogel at different temperatures and to optimize printability [8,9,20]. Usually, the higher the material viscosity, the higher the printability, at least up to a viscosity value in which internal pressures generated can damage cells. Additionally, other works analyze how temperature affects the bioink viscosity [21–24]. All of them conclude that viscosity decreases when temperature is increased in most bioprinting materials, such as GelMA, alginate and, many other thermo-responsive materials. However, each bioink must be studied separately to quantify these rheological changes with temperature. Therefore, the behavior of the bioink flowing inside a nozzle is an important aspect to determine, but difficult to achieve with experimental tests, mainly due to the small size of the nozzles, which are hardly sensorized without any scaling technique. In this sense, experimental tests of bioink behavior are usually focused on bioprinting results, such as printability, shape fidelity, or cell viability, but not so commonly on the parameters of the process that can influence the results, such as shear stress, pressure or velocity, during bioprinting. This approach is far from ideal due to the high number of test iterations and economic costs associated, so computational simulation is proposed as a very helpful tool to perform parametrical series of studies [25,26]. Computational Fluids Dynamics (CFD) are widely used to obtain flow behavior in simple (e.g., pipes) or more complicated (e.g., cranial aneurysms) designs [27]. Specifically, CFD can calculate microfluidics inner parameters, such as velocity, pressure or shear stress, which are experimentally difficult to measure. It is well known that nozzle inner pressures, and more specifically shear stress, have a major impact on cell viability [28]. Therefore, the higher the shear stress is, the lower the cellular viability. Specifically, Blaeser et al. [29] determined that cells affected by low shear stress (<5 kPa) have high cellular viability (up to 96%), while increasing the shear stress (5-10 and >10 kPa) results in lower cellular viability (91% and 76%, respectively). Other authors have performed several computational simulations to study shear stress [30], non-commercial nozzle geometries [31–33], different bioprinting materials [34] or tuned rheological properties of specific materials [26,35]. It is important to note that printability and shape fidelity are bioprinting measures which are highly dependent on the dynamic relationship between nozzle and printing substrate. For this reason, several studies analyze parameters such as the separation between nozzle and printing substrate and the XY-plane speed of the nozzle while printing in detail [9,30,34]. These bioprinting settings will affect the bioink filament width that directly relates not only to shape fidelity, but also to filament width stability. In this sense, we understand stability, such as the property of a bioink, produces a well-known width of filament that could be maintained during the whole bioprinting process. A computational simulation of this dynamic interaction is highly complex, so, in this study, the interaction with the printing substrate is removed and a preliminary analysis of the bioink filament stability on the air is proposed.

Computational simulations are used to study several inner nozzle parameters of the nozzle in two main fields: either referring to the effect of nozzle geometry with fixed bioink properties [31–33,36,37] or to the bioink behavior with fixed geometry [26,30,34,38–40]. However, very few authors also perform simulations and studying cells deformation during the bioprinting procedure [37]. Some authors performed more complex simulations to study droplet formation using a Two-Phase Level Set [40,41] and to analyze the filament deposition and the final bioprinted shape using a surface tension model [26]. Liravi et al. [40] and Smanipour et al. [41] used COMSOL Multiphysics to simulate the generation of droplets with a 27G conical tip and a custom-made micro-encapsulation device, respectively. Both studies focused on obtaining a realistic geometrical droplet compared to an experimental test. Thus, inner nozzle flow parameters (pressure, velocity or shear stress) were not reported, although

these parameters are essential to determine whether cells survive. Despite using the same mathematical model, none of them reported the numerical methods used, so the reproducibility of their research is hindered. Furthermore, three main differences can be noticed between both works. Firstly, they provide different levels of detail for the mesh. Liravi et al. [40] used a very specific mesh generation with a remeshing procedure developed by Wilkes et al. [42] to properly generate droplets. On the contrary, Samanipour et al. [41] did not even mention the mesh they generated for their simulations. Secondly, the characterization of the material is done under different fluid assumptions. Liravi et al. [40] used a Carreau–Yasuda potential model to fit the rheological data of a non-Newtonian material, while Samanipour et al. [41] used a constant value for viscosity for simplicity. The former method is used to fit all data, at the expense of using a complex equation, while a simpler Potential Law cannot fit very low or very high shear rate values. Lastly, regarding materials, Liravi et al. [40] used several concentrations of a polysiloxane-based hydrogel extruded into the air. Samanipour et al. [41] used a GelMA hydrogel extruded into oil. Therefore, all previous simulations analyze the behavior of non-commercial bioinks and, as far as the authors know, no previous computational analysis has been performed for Cellink Bioink. This bioink is made of alginate with nanocellulose fibers and some authors have experimentally demonstrated the adequate bioprinting properties of this type of bioink (good rheological behavior, cellular viability or mechanical response) [43–45]. Among those authors, Müller et al. have also performed additional CFD computational simulations to study pressure and shear stress inside a needle [46].

Hence, the objective of this work is to analyze the Cellink Bioink behavior while bioprinting using computational simulations. Specifically, the pressure, velocity, and shear stress of this bioink are studied using three temperatures (15, 25, and 37 °C) and three conical tips' geometries (20, 22, and 25G) as inlet parameters. Additionally, an analysis of the bioink filament volume is performed to measure its stability undero nine different combinations of temperatures and geometries in simple conditions.

2. Materials and Methods

2.1. Computational Model

Three geometrical models were created and simulated in COMSOL Multiphysics 5.4a (COMSOL Inc., Burlington, MA, USA, 2018) through a 2D axisymmetric model and a Two-Phase Flow level set interface. Commercial 20G, 22G, and 25G conical tip geometries (Figure 1) were selected for simulations. A 22G conical tip is the recommended tip for Cellink Bioink by Cellink in its bioprinting manual [46], while 20 and 25G were selected because they are the bigger and smaller most used sizes after 22G. All conical tips were modelled after experimental measurements using a caliper. The geometrical model and its measurements can be seen in Figure 2. left, where X is 0.30, 0.20, and 0.13 mm for 20, 22, and 25G, respectively. The conical tip was modelled using a trapezium and a rectangle, while the air was composed of a rectangle and a trapezium. Two different domains were considered in the geometrical model. The first domain was related to the nozzle where the hydrogel was placed, and the second domain was the outside of the nozzle and corresponds to the air where the bioprinting material was ejected (Figure 2 right). Models were meshed using COMSOL-optimized mesh generation for fluid dynamics with 2D triangular elements obtaining a total of 6353 elements with sizes ranging from 0.015 to 0.335 mm. The average skewness mesh quality is 0.9121 with a minimum value of 0.5715.

Figure 1. Cellink bioprinting conical tips. From left to right: 20, 22, and 25G. Reproduced with permission from Cellink®.

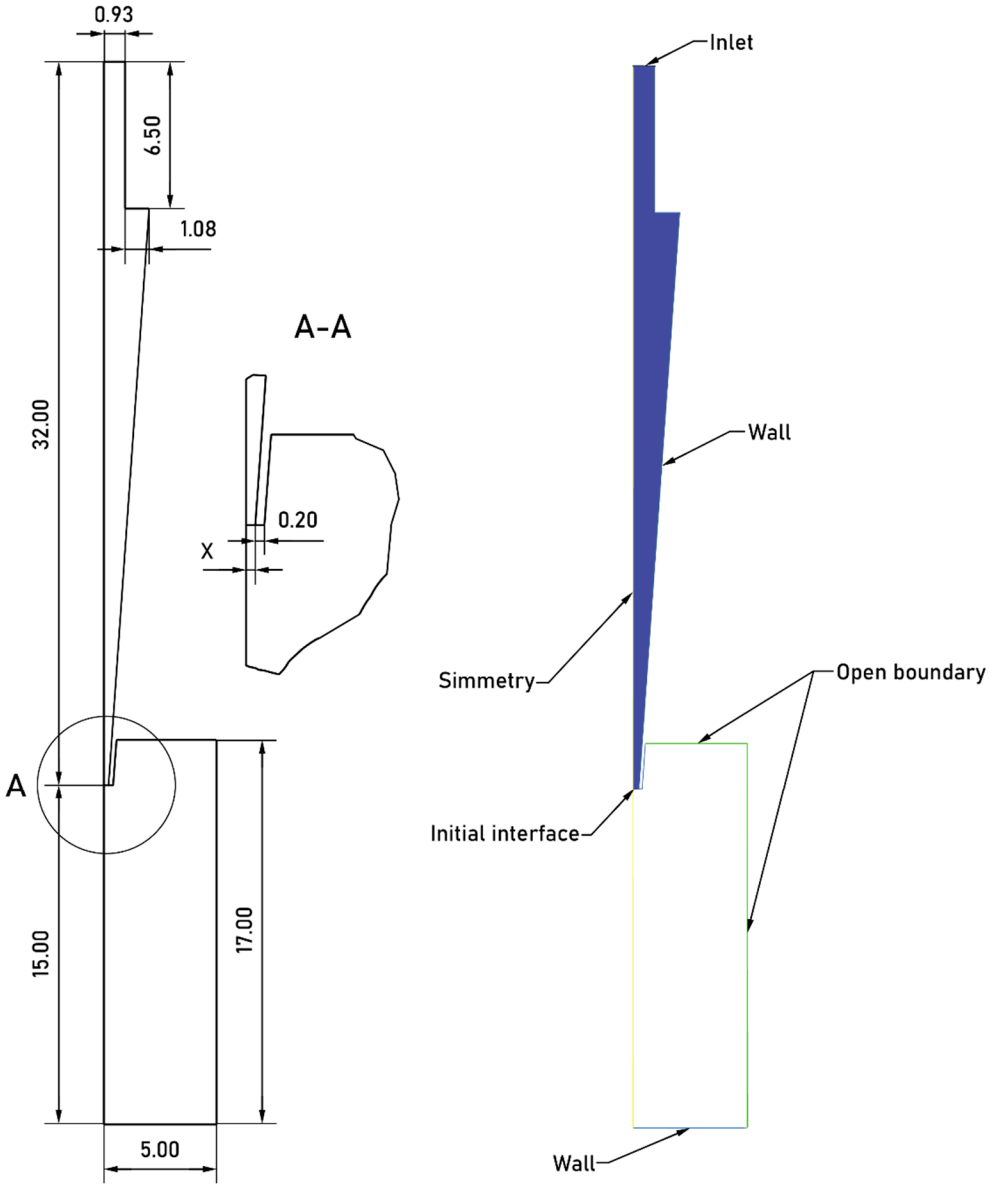

Figure 2. Representation of models' geometry, in millimeters, based on real measures of a commercial conical tip where X = 0.30, 0.20, and 0.13 mm for 20, 22, and 25G, respectively (**right**). Representation of bioink domain (light grey) and air domain (dark grey) with all boundary conditions (**left**).

Level Set method is a Eulerian transport method capable of capturing the interface of two fluids and the changes of the interface because of motion. This method couples the track of the interface with a fluids dynamic of each fluid, expressed by incompressible Navier–Stokes equations

$$\rho\frac{\partial u}{\partial t} + \rho\,(u\cdot\nabla)u = \nabla\cdot\left[-pI + \mu\left(\nabla u + \nabla u^T\right)\right] + F_{st} + \rho g \tag{1}$$

$$\nabla\cdot u = 0 \tag{2}$$

where ρ is the density, u is the speed of the fluid, p denotes the pressure, I is the identity matrix, μ is the fluid viscosity, g is the gravity, and F_{st} is the surface tension force calculated as

$$F_{st} = \nabla\cdot\left[\left(\sigma\left(I - \frac{\nabla\phi}{|\nabla\phi|}\left(\frac{\nabla\phi}{|\nabla\phi|}\right)^T\right)\right)\delta\right] \tag{3}$$

where σ is the surface tension, ϕ is the contour line of the gas–liquid two-phase flow interface, and δ is the Dirac delta function formulized as follows

$$\delta = |\phi(1-\phi)||\nabla\phi| \tag{4}$$

Initially, the flow is assumed to be laminar, but a posterior verification is needed after simulation by calculating the Reynolds number.

The material used for the simulations was the commercially available Cellink Bioink, composed of alginate and nanocellulose fibers, with a density equal to 1000 kg/m^3. Its surface tension was measured and calculated using a KRUSS G20/DSA10 drop shape analyzer, obtaining a value of 55.8 mN/m. Additionally, its viscosity/shear rate at 15, 25, and 37 °C was provided by Cellink and fitted to a simple viscosity Potential Law

$$\mu = m\left(\dot{\gamma}\right)^{n-1} \tag{5}$$

where μ is the dynamic viscosity (Pa·s), m is the fluid consistency index, $\dot{\gamma}$ is the shear rate (s^{-1}), and n is the flow behavior index. The selection of a simpler viscosity law pursues minimizing the computational cost, as long as the shear rate is within the proper values. The fitting parameters and goodness of the fit are listed in Table 1 and in Figure 3.

Table 1. Consistency index (m) and flow behavior index (n) of Cellink Bioink at 15, 25, and 37 °C.

Parameters	15 °C	25 °C	37 °C
m ($Pa{\cdot}s^n$)	92.735	102.53	87.906
n (adimensional)	0.146	0.170	0.208
Goodness of the fit (R^2)	0.9985	0.9925	0.9906

All bioink data were introduced in COMSOL as a user defined material and air data was obtained from COMSOL material library.

In the Level Set method, Cellink Bioink is expressed by ϕ = 0, the air is expressed by ϕ = 1, and the level set interface (transition area between both materials) is expressed by ϕ = 0.5. The level set equation can be seen as the volume percentage of liquid in the gas-liquid two-phase flow [47].

Density and viscosity of the involved material can change in the interface following the level-set functions

$$\rho = \rho_{air} + (\rho_{bioink} - \rho_{air})\phi \tag{6}$$

$$\mu = \mu_{air} + (\mu_{bioink} - \mu_{air})\phi \tag{7}$$

The track of the level set interface is described in the following equation when it moves under the velocity field u

$$\frac{\partial \phi}{\partial t} + u \cdot \nabla \phi = 0 \tag{8}$$

Only the normal component of the velocity is needed because the level-set method considers the interface movement to be normal to itself. Therefore, Equation (8) can be reformulated as follows

$$\frac{\partial \phi}{\partial t} + u_n \left| \nabla \phi \right| = 0 \tag{9}$$

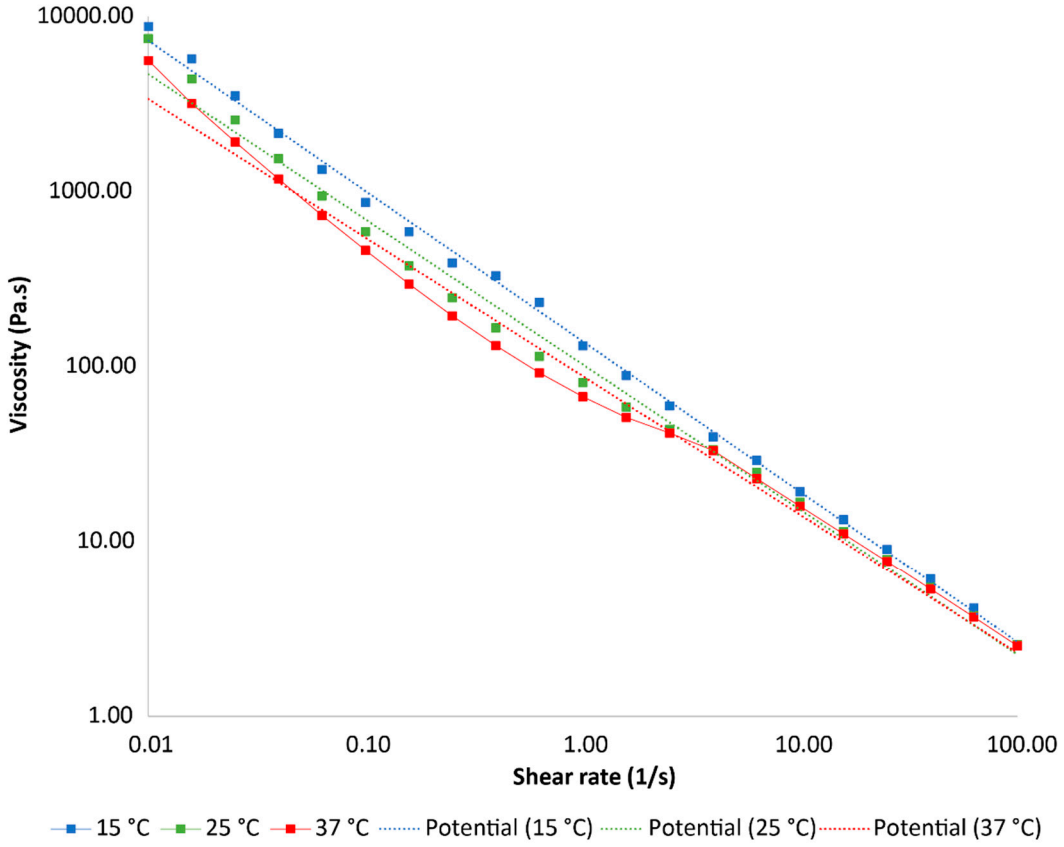

Figure 3. Cellink Bioink rheological data. Reproduced with permission of Cellink®.

The Level Set method needs its function to be a distance function within all simulation to depict the interface. To assure a correct depict of the interface, numerical reinitialization and stabilization terms are added to the level set equation. Therefore, the non-conservative reinitialized level set function can be formulated as

$$\frac{\partial \phi}{\partial t} + u \cdot \nabla \phi = \gamma \nabla \left(\epsilon \nabla \phi + \phi (1 - \phi) \frac{(\nabla \phi)}{\left| \nabla \phi \right|} \right) \tag{10}$$

where ϕ is the contour line of the gas-liquid two-phase flow interface, γ is the reinitialization parameter (approximately the maximum value of the velocity field), and ϵ is the interface thickness parameter (usually half of the mesh size in the region). Here, the bioprinting material corresponds to the domain where $\phi < 0.5$, and air corresponds to the domain where $\phi > 0.5$.

Boundary conditions were set as shown in Figure 2, they were stablished taking into account that all simulations are a 2D axisymmetric simulation and to make possible a realistic shear-thinning non-Newtonian flow. In this sense, the laminar flow inlet was set as a full developed flow, described with

the following equations to assure tangential flow component on the boundary is zero (Equation (11)) and to set the real inlet value (Equation (12))

$$u - (u \cdot n)n = 0 \tag{11}$$

$$[-pI + K] = -p_{in}n \tag{12}$$

where p is the user average pressure (N/m^2), in our simulations 15 kPa, as recommended by Cellink in their bioprinting manuals for Cellink Bioink [46], K is the viscous stress (N/m^2), and p_{in} is the real inlet pressure (N/m^2).

The outlet boundary condition was set as an open boundary condition with no normal stress to allow bioprinting material to fill this domain and air to leave. Additionally, wall boundaries were set with a non-slip condition, which means that the velocity on the walls is zero, and level set interface in the wall is described by

$$n \cdot \left(\epsilon \nabla \phi - \phi(1 - \phi) \frac{\nabla \phi}{|\nabla \phi|} \right) = 0 \tag{13}$$

Because the simulation is an 2D axisymmetric simulation, a symmetry boundary condition was set, as shown in Figure 2. It was modelled as a combination of Neumann and Dirichlet boundary conditions, allowing flow to not penetrate this boundary, and vanishing shear stress for an incompressible flow

$$u \cdot n = 0 \tag{14}$$

$$\left(-pI + \mu \left(\nabla u + (\nabla u)^T \right) \right) n = 0 \tag{15}$$

2.2. Simulation

Nine simulations of 10 s with a 1 ms step were carried out for each geometry and temperature. Each simulation was composed of two study steps: Phase Initialization and Time-Dependent. The Phase Initialization step is in charge of obtaining all initial values of the Level Set method on every mesh element. In this sense, Phase Initialization is solved in COMSOL using the distance to the initial interface, D_{wi} (m), and initializes the level set variable ϕ to ensure a smoothly variation between 0 and 1 (maximum and minimum values) and to minimize numerical instabilities. Then, this initial level set value is translated to the Time-Dependent step using the following expressions for the two different domains

$$\phi_0 = \frac{1}{1 + \frac{e^{D_{wi}}}{\epsilon}} \tag{16}$$

in domains initially filled with bioprinting material, and

$$\phi_0 = \frac{1}{1 + \frac{e^{-D_{wi}}}{\epsilon}} \tag{17}$$

in domains initially filled with air, where ϕ is the domain reference (volumetric fraction), and ϵ is the interface thickness (m).

For the Phase Initialization step, a stationary solver was used to calculate the level set initial values that later were used as t = 0 values by the time-dependent solver of the Time-Dependent step. Both the Phase initialization and the Time-Dependent steps used a Newton non-linear method in a fully coupled solver with a Parallel Direct sparse Solver (PARDISO). The Newton non-linear method is in charge of the successive iterative calculation of all coupled Fluids Dynamics and Level Set formulas described before. This method evaluates all non-linear expressions and the Jacobean on each iteration and assures that the calculation error between successive iterations is below the user tolerance (set at 10^{-6}). If the error is higher than tolerance, the damping factor is automatically changed, and the time

step is reduced. The time step is calculated using a Backward Euler BDF method which is known for its stability and is the most recommended one for fluid transportation in COMSOL.

The PARDISO is a solver based on LU decomposition that tries to improve the sequential and parallel sparse numerical factorization performance. This method can use all computer cores to perform parallel calculations, reducing the simulation time to the detriment of computer expenditure.

3. Results and Discussion

Reynolds numbers were calculated for all simulations obtaining a maximum value of the order of 10^{-4}, which means that the initial assumption of laminar flow is correct. In the same way, the shear rate of all simulations has been checked, ranging from 0.1 to 155 1/s. Therefore, the Cellink Bioink behavior curve can be modelled using the Potential Law.

All simulation errors were measured in the velocity field. The error between successive time steps was below 10^{-6} in the 18th step with a later average error of 10^{-13}. To achieve these low errors, a very small-time step (approximately 10^{-6} s) is calculated by the BDF method, ranging the simulation time between 3 and 10 h.

3.1. Outlet Pressure

Simulated outlet pressure was measured using a line probe at the very end of the nozzle, specifically in the initial gas–liquid interface. Figure 4 shows all pressures for 20, 22, and 25G conical tips at 15, 25, and 37 °C.

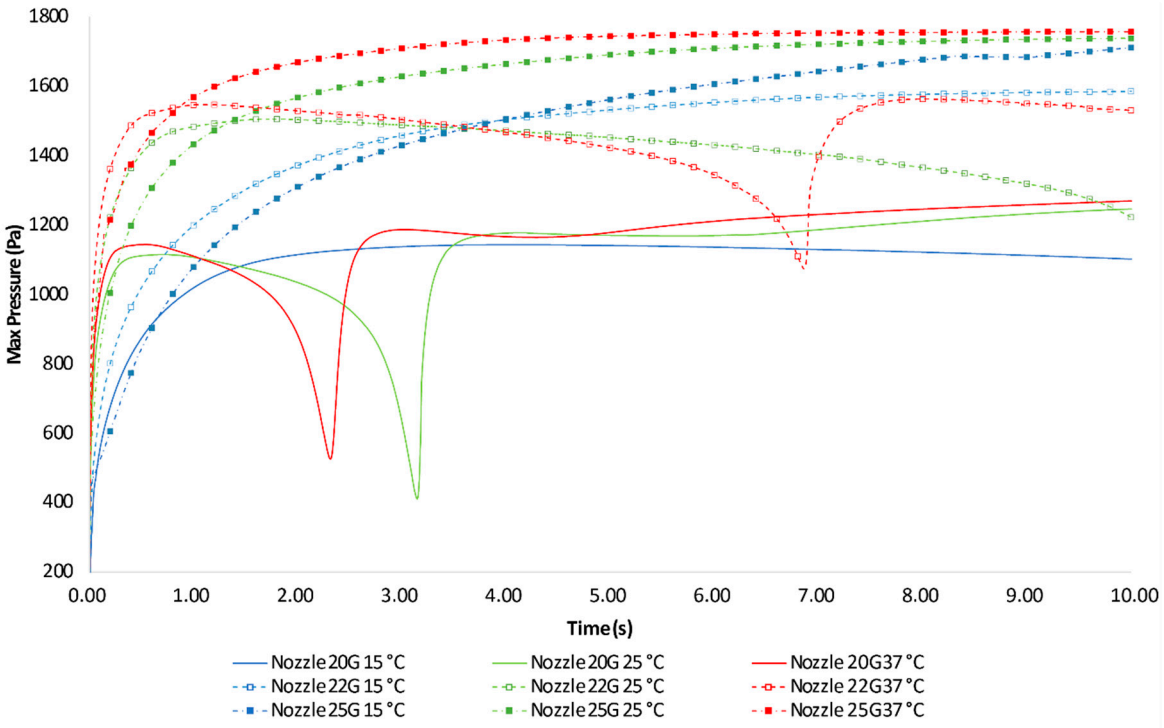

Figure 4. Maximum outlet pressure for 20, 22, and 25G conical tips using Cellink Bioink at 15, 25, and 37 °C.

Three out of nine simulations present a low-pressure peak in their temporal evolution of maximum outlet pressure (25 and 37 °C for 20G and 37 °C for 22G). Additionally, the outlet pressure of 22G conical tip at 25 °C decreases at the end of the simulation, which implies that a low-pressure peak is being formed beyond the 10 s, similarly to the peaks in the other simulations. In this sense, to properly analyze and compare the pressure behavior of all simulations, a set of relevant points are identified. These points are: (1) the maximum value before the low-pressure peak, (2) the minimum pressure

value, (3) the stable pressure value just after the peak, and (4) the pressure value at the end of the simulation. All plots were analyzed to identify these key points when available (for plots without peak, only the value at the end of the simulation is provided) and their pressure values are shown in Table 2.

Table 2. Maximum outlet pressure values (Pa) and time (s).

Geometry	Temp	Before Peak (Time)	Peak (Time)	After Peak (Time)	End Simulation (Time)
20G	15 °C	1143.6 (4.10)	-	-	1102.3 (10.00)
	25 °C	1115.3 (0.67)	409.4 (3.14)	1178.3 (4.10)	1246.9 (10.00)
	37 °C	1144.3 (0.52)	526.8 (2.31)	1187.6 (3.01)	1269.9 (10.00)
22G	15 °C	-	-	-	1585.5 (10.00)
	25 °C	1505.2 (1.72)	-	-	1222.4 (10.00)
	37 °C	1547.2 (1.13)	1074.9 (6.86)	1563.2 (8.01)	1530.9 (10.00)
25G	15 °C	-	-	-	1711.3 (10.00)
	25 °C	-	-	-	1738.2 (10.00)
	37 °C	-	-	-	1757.1 (10.00)

It might be expected Cellink Bioink at 37 °C to have the lowest pressure for each one of the different conical tips. This supposition is based in the viscosity analysis, as a low viscosity fluid is supposed to provoke lower inner pressures when compared to a higher-viscosity fluid for the same conical tip. Specifically, in bioprinting materials, other authors as Bartnikowski et al. [48] have checked that hydrogels' viscosity usually decreases when temperature increases. However, there are some cases, such as Pluronic, that an increment in temperature provokes an increase in viscosity. This specific material contains (poly (ethylene oxide))$_{100}$-(poly (propylene oxide))$_{65}$-(poly (ethylene oxide))$_{100}$. At a low temperature, it is an individual block of copolymers but when temperature increases, its internal structure changes and forms micelles that increase its viscosity [49]. In our case, Cellink Bioink is composed by alginate and nanocellulose fibers. Its behavior was analyzed in several works [26,43,45,50] and they all determine that the normal behavior of this kind of bioink is that the higher the temperature is, the lower the viscosity. Therefore, considering Table 2 and Figure 4, it is clear that this expected behavior is not obtained by all but one of the analyzed conical tips. More specifically, 22G conical tip is the only geometry where outlet pressure is higher at 15 °C than at 25 and 37 °C. This unexpected behavior is caused by the different inlet volumetric flow in all simulations. In this sense, the total extruded volume of Cellink Bioink along the time is shown in Figure 5. Additionally, the total volume values referring to the key points defined before can be seen in Table 3. Therefore, when pressure is selected as simulation inlet parameter, the volumetric flow cannot be further controlled. It depends on the fluid viscosity and the inner geometry where the fluid flows.

Therefore, two main considerations can be extracted from the pressure results. On the one hand, the geometry can change the outlet pressure value. In general, the bigger the outlet diameter is (the smaller the conical tip gauge), the lower the pressure is (Figure 4). On the other hand, the temperature has a slight influence on pressure for the same geometry. Despite different bioink temperatures leading to different pressures, the average differences are around 600 Pa, so they can be considered negligible.

In order to properly compare our pressure results with those from bibliography, we have selected the values not considering excluding the low-pressure peak values. Thus, our maximum pressure values vary between 1143 and 1757 Pa. As far as the authors know, Reid et al. [33] have performed the only study that analyzed this pressure under experimental settings. They found that pressure ranged from 101 to 107 kPa using *"a fluid with similar properties to blood"*, such as the bioink, but further information is not provided. They focused on the geometrical optimization of the inner nozzle geometry using different shapes and lengths and set up the inlet flow at 0.1 mm^3/s. In this regard, the lack of information about the used bioink makes difficult to compare results. However, it seems that their high-pressure values are caused by the very small outlet diameter (60 μm) used.

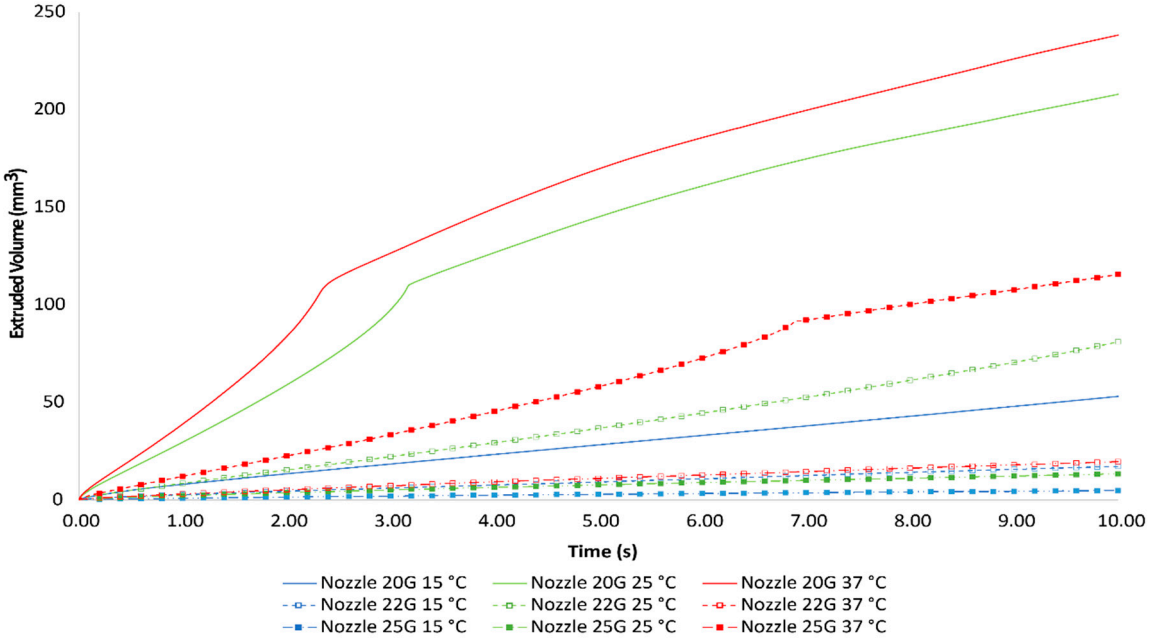

Figure 5. Total extruded volume for 20, 22, and 22G conical tips using Cellink Bioink at 15, 25, and 37 °C.

Table 3. Cellink Bioink extruded volume (mm^3) and time (s).

Geometry	Temp	Before Peak (Time)	Peak (Time)	After Peak (Time)	End Simulation (Time)
20G	15 °C	-	-	-	53.22 (10.00)
	25 °C	-	107.06 (3.14)	-	208.02 (10.00)
	37 °C	-	105.31 (2.31)	-	238.33 (10.00)
22G	15 °C	-	-	-	17.31 (10.00)
	25 °C	-	-	-	81.20 (10.00)
	37 °C	-	90.28 (6.86)	-	115.67 (10.00)
25G	15 °C	-	-	-	5.00 (10.00)
	25 °C	-	-	-	13.51 (10.00)
	37 °C	-	-	-	19.78 (10.00)

Although Lee et al. [51] determined that alginate bioinks are not thermo-responsive and the viscosity variation is not noticeable, our results (Table 3) show that temperature has an important influence on bioprinting procedure. For a specific conical tip, an increase in temperature provokes the bioink viscosity to decrease, therefore generating a higher flow rate. Controlling the amount of extruded material is one of the key points in a successful bioprinting procedure. Most commercial bioprinters are pneumatic-driven and their main limitation is that the bioink flow cannot be precisely controlled [52]. To create any tissue, it is necessary to deposit a determined amount of material in a certain point, so, if temperature influences the bioink flow, other printing parameters, such as XY-speed, must be carefully selected to achieve proper results.

As mentioned before, there are three simulations with low-pressure peaks and a fourth one where a peak is foreseen. Comparing Figures 4 and 5, the low-pressure peaks are produced at the exact time an abrupt change in volumetric flow is observed. Those peaks are produced at different times depending on the geometry and the temperature: 2.31, 3.14 and 6.86 s for 20G at 37 °C, 20G at 25 °C, and 22G at 37 °C, respectively. At those instants, an initial droplet is formed (Figure 6), which would eventually fall, taking into account that the cross-area is reduced in such way that it can be considered that the droplet will fall. This droplet creation also depends on the distance to the printing substrate. In the light of the presented results, it seems that none of the simulated temperature/geometry configurations at 15 kPa will form a stable filament but droplets. Simulation time (t = 10 s) is not enough to even

generate the initial droplet at the lowest temperature (15 °C) or lowest inner diameter (25G). The four images in Figure 6 show the simulations where a droplet is generated and drops (A, B, C) or is about to drop (D). Table 3 shows that the bioink volume to produce a falling droplet varies depending on the geometry. In this sense, the total volume of Cellink Bioink hanging from the conical tip is around 106 mm^2 on average for 20G, and 90 mm^2 for 22G. The formation of droplets depends on factors such as the volumetric flow, the viscosity of the material, the cross-section area and, in particular for hydrogels, the distance between the nozzle tip and the printing substrate. In our simulations, droplets are formed because two main reasons. First, both 20 and 22G have the same wall thickness (0.2 mm, Figure 2), but the total cross area of the conical tip outlet is 0.50 and 0.38 mm^2 for 20 and 22G, respectively. Since the total droplet volume before falling is dependent on the cross-area in contact as well as the surface tension and this is constant, the cross-area limits the maximum volume of the droplet. Secondly, the distance to the printing substrate, defined as "h" by He et al. [9], usually varies from µm to few mm in a standard bioprinting procedure, but we have set a larger h in our simulations to check whether Cellink Bioink is capable of creating a stable filament on the air. Therefore, in Figure 6A,B, it is shown the simulations at the exact time (3.14 and 2.31 s, respectively) when a visible reduction in the cross-area near the conical tip of 20G at 25 °C and 37 °C that will cause the droplet fall. Additionally, in Figure 6D, the falling droplet of 22G at 37 °C in t = 6.86 s is represented, while Figure 6C shows the 22G at 25 °C simulation in t = 10 s, in which the total extruded volume is not enough to generate a falling droplet. According to our results, none of the analyzed combinations can generate a stable filament flow on the air, due to either the generation of droplets or an insufficient extruded volume. Therefore, other printing parameters related to these printability and shape fidelity features, such as h and XY-plane speed, should be correctly selected to create such stable filament flow.

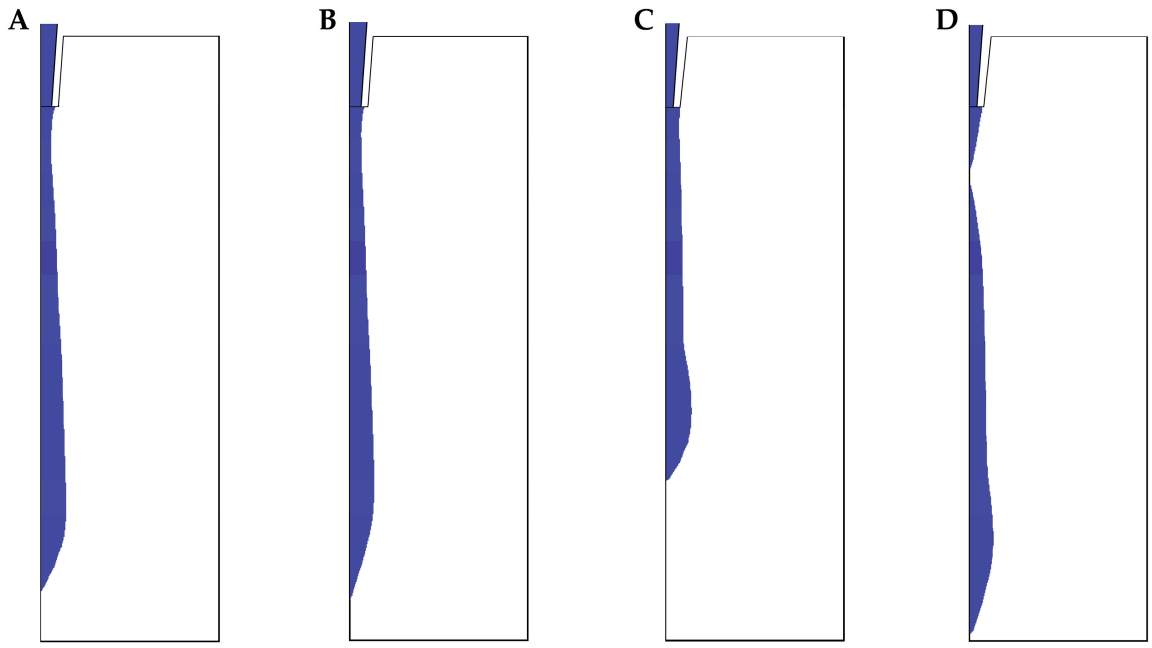

Figure 6. Volume fraction of Cellink Bioink. (**A**) 20G at 25 °C in t = 3.14 s, (**B**) 20G at 37 °C in t = 2.31 s, (**C**) 22G at 25 °C in t = 10.00 s and (**D**) 22G at 37 °C in t = 6.86 s. Blue color represents Cellink Bioink and white color represents the air.

Finally, Figure 4 shows an increase in pressure since 3.01 and 4.10 s in 20G at 37 °C and 20G at 25 °C, respectively, until the end of the simulations. This final increase in pressure is provoked by the material accumulation on the printing substrate. This accumulation reaches de conical tip and causes the rise of pressure to continue to the extruding material. Therefore, to the existing extrusion pressure, the force needed to push away the already extruded material must be added.

3.2. Outlet Velocity

Simulated maximum outlet velocity was measured using the same probe as in pressure, at the very end of the nozzle. Figure 7 shows the maximum velocity for 20, 22, and 25G conical tips for 15, 25, and 37 °C along the time.

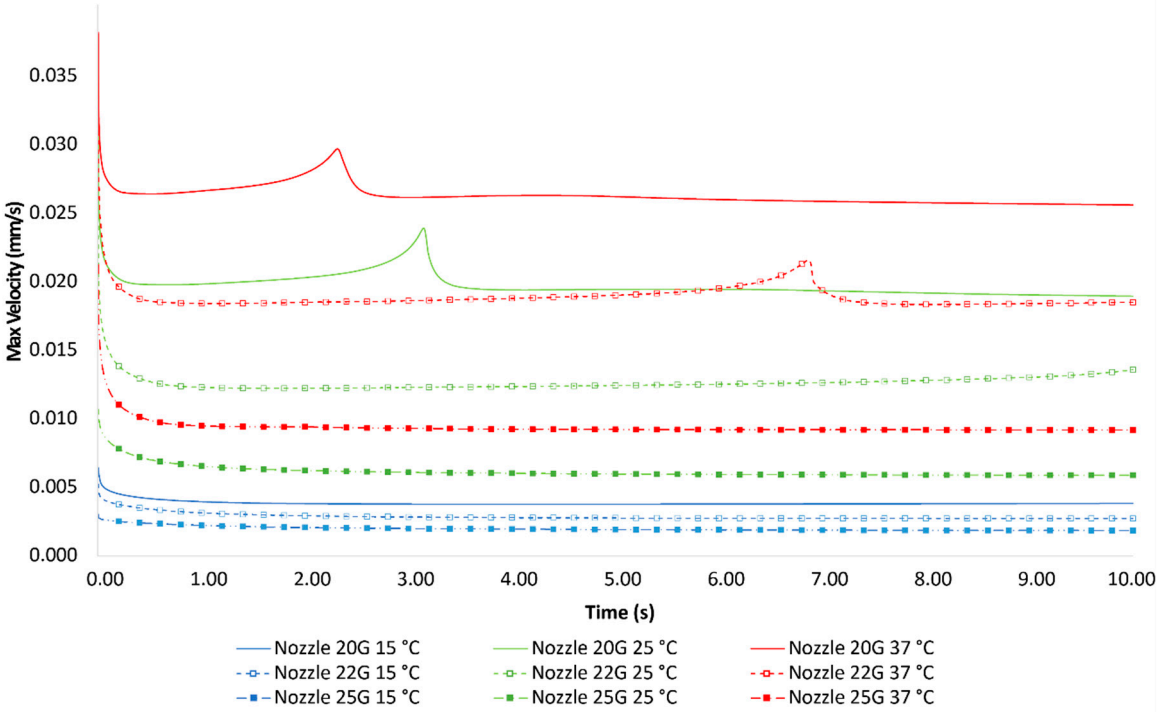

Figure 7. Maximum outlet velocity of 20G, 22G, and 25G conical tips using Cellink Bioink at 15, 25, and 37 °C.

Additionally, Table 4 presents all velocity values in the previously defined key points. It can be observed that there are high-velocity peaks produced at the same time as the low-pressure peaks. The velocity increment is produced by the droplet material pulling the bioink outside the nozzle. When the droplet is completely separated from the nozzle, the velocity peak disappears, and the previous value is restored.

Table 4. Maximum outlet velocities values (cm/s) and time (s).

Geometry	Temp	Before Peak (Time)	Peak (Time)	After Peak (Time)	End Simulation (Time)
20G	15 °C	0.38 (4.10)	-	-	0.38 (10.00)
	25 °C	1.98 (0.67)	2.39 (3.14)	1.94 (4.10)	1.89 (10.00)
	37 °C	2.64 (0.52)	2.97 (2.31)	2.62 (3.01)	2.56 (10.00)
22G	15 °C	-	-	-	0.27 (10.00)
	25 °C	1.22 (1.72)	-	-	1.36 (10.00)
	37 °C	1.84 (1.13)	2.19 (6.86)	1.84 (8.01)	1.85 (10.00)
25G	15 °C	-	-	-	0.19 (10.00)
	25 °C	-	-	-	0.59 (10.00)
	37 °C	-	-	-	0.92 (10.00)

It would be expected that the outlet velocity depends on the outlet geometry for a certain inlet flow, as defined by continuum equation. In this sense, and as explained before, an inlet boundary condition of 15 kPa makes the bioink inlet flow to be dependent on its viscosity and the nozzle

geometry. This dependency results from a variability in the flow for all simulations, as can be seen in Figure 5. Similar to the findings in the pressure, there are two important considerations for velocity. Firstly, for the same geometry, velocity changes with temperature. As explained before, the lower the temperature is, the lower the viscosity and the higher the extruded volume. An increase in volumetric flow leads to an increase in velocity according to continuum equation when cross-area remains constant. Therefore, temperature changes the extrusion velocity. Lastly, the geometry has also an important influence on velocity, and this influence is higher when the conical tip gauge increases. As shown in Figure 7 the influence of temperature on velocity is higher at lower gauges, while at higher gauges the effect of temperature is reduced and the cross-section area reduction plays a major role.

Regarding to other authors velocities, they obtained different results: velocities equal to 5.50 and 7.20 cm/s for a 60 µm diameter conical and needle tip, respectively [33], or 36.70 cm/s for a 28G gauge needle [36]. Again, differences between their results and our simulations might be explained by differences in viscosities, which cannot be assured, as authors do not provide this parameter for their bioink. Nevertheless, our results confirm that differences in cross-area have an important influence on velocities.

3.3. Shear Stress

Simulated shear stress is measured in the whole inner extruder domain using a surface probe. Maximum shear rate values are presented in Figure 8 and Table 5.

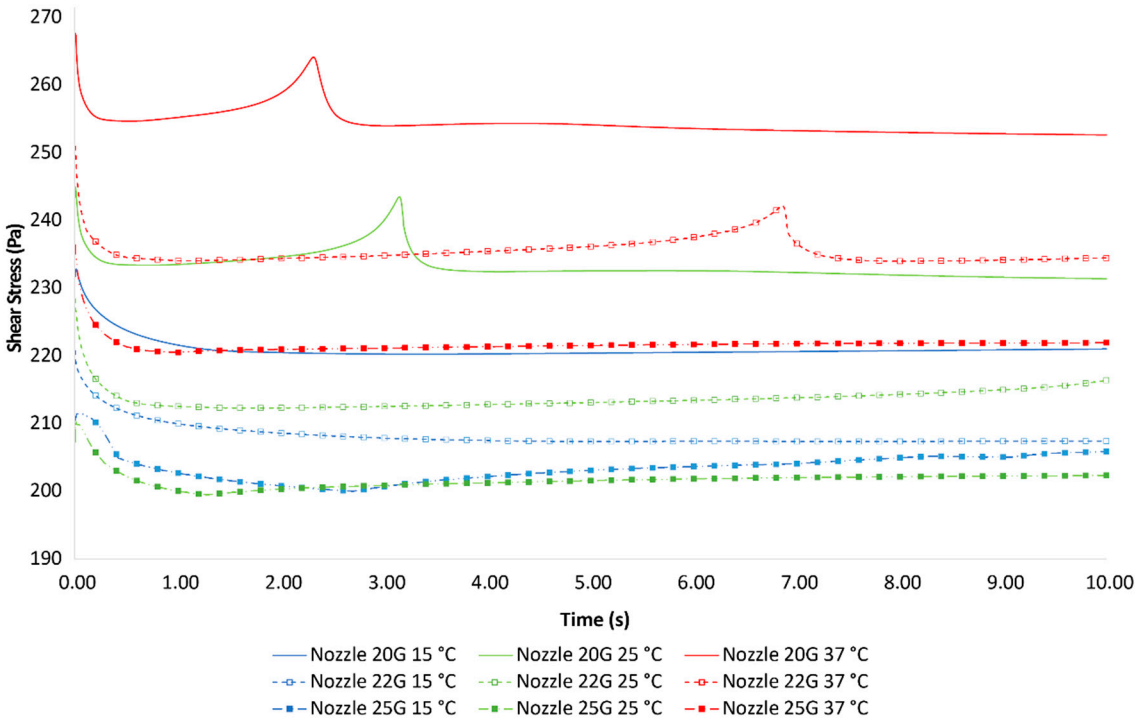

Figure 8. Maximum shear stress of 20, 22, and 25G conical tips using Cellink Bioink at 15, 25, and 37 °C.

Since shear stress depends on shear rate, and shear rate depends on velocity, it might be expected that shear stress behaves similarly to velocity. In any case, the analysis of shear stress must be done carefully for non-Newtonians fluids, as the variations in viscosity with shear rate might change the shear stress behavior. As can be seen in Figure 8, both shear stress and velocity have a similar temporal behavior.

Results show that shear stress varies with temperature and geometry. For a defined geometry, the shear stress decreases when temperature increases, and the temperature influence is reduced when the conical tip gauge increases. Additionally, high-shear stress peaks appear at the same time as

pressure or velocity peaks. Nevertheless, an odd behavior of 25G at 15 °C, and 25G at 25 °C can be found, with an increment of shear rate at the end of the simulation, which might be caused by the high viscosity of the material at those temperatures where the bioink has a low velocity (shear rate).

Table 5. Maximum shear rate values (Pa) and time (s).

Geometry	Temp	Before Peak (Time)	Peak (Time)	After Peak (Time)	End Simulation (Time)
20G	15 °C	220.34 (4.10)	-	-	220.04 (10.00)
	25 °C	233.41 (0.67)	243.48 (3.14)	232.46 (4.10)	231.42 (10.00)
	37 °C	254.71 (0.52)	264.16 (2.31)	254.01 (3.01)	252.66 (10.00)
22G	15 °C	-	-	-	207.41 (10.00)
	25 °C	212.32 (1.72)	-	-	216.41 (10.00)
	37 °C	234.10 (1.13)	242.16 (6.86)	234.01 (8.01)	234.48 (10.00)
25G	15 °C	-	-	-	205.88 (10.00)
	25 °C	-	-	-	202.35 (10.00)
	37 °C	-	-	-	221.96 (10.00)

The measurement of shear stress is done in the whole domain, so the maximum value may not be found in a fixed position. However, Liu et al. [30] observed that maximum shear stress is placed at the very tip of the conical tip nozzle. In this regard, the shear stress distribution in all simulations is very similar to the 22G at 37 °C (Figure 9).

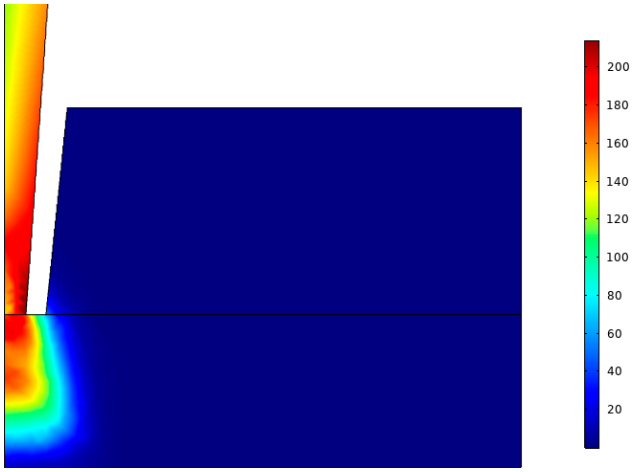

Figure 9. Shear stress distribution (Pa) at 37 °C.

Many authors agree that shear stress is one of the main parameters to analyze and control in order to reduce cell death during the bioprinting process. Similarly to the finding of Yan et al. [28], our results specifically confirm that increasing pressures or increasing outlet diameter provoke wall shear stress to increase. On the contrary, our simulations do not coincide with Liu et al. [30], as we obtain lower shear stress with higher viscosity of the bioink. This different behavior might be caused by the different inlet used in our simulations and their experiments, because Liu et al. used a constant mass flow, while we have used a constant pressure. Müller et al. [45] also studied the shear stress using several nozzles with a very similar bioink, but in the same way as with Liu et al., their results are not directly comparable to ours due to the different geometries and inlet pressures. Hence, previous experimental tests are hardly comparable due to different boundary conditions or scarce definition of bioprinting parameters. On the other hand, shear stress can be found ranging from approximately 200 Pa to 20 kPa. In this sense, our results are quite similar to those obtained by Li et al. [37]. Specifically, those related to an inlet flow of 0.015 mL/s using an alginate hydrogel (0.41 Pa·s).

According to Blaeser et al. [29], shear stresses below 5 kPa do not have a harmful effect on cells (cellular viability over 96%). Although our results show high variability in shear stress values, all of them remain below 5 kPa. Therefore, low damage effect on cells is expected, which allows for high cellular viability.

4. Conclusions

In this work, several simulations have been done to study the impact of temperature and geometry in a commercial bioink: Cellink Bioink, its rheological data and inlet pressures were provided by the company bioprinting protocols. The simulation results demonstrated the suitability of this commercial bioink to be used in micro-extrusion bioprinting techniques, regardless of the temperature or the conical tip used (15, 25, and 37 °C and 20, 22, and 25G). However, it is recommended to use this bioink at 37 °C, not with the aim of having a minimum shear stress, but in order to obtain the higher volumetric flow. A higher volumetric flow leads to higher bioprinting speed, so cells are under pressure for a shorter time. Additionally, shear stress obtained from simulations forecasts a proper cellular viability at all temperatures, according to previous studies for values under 5 kPa.

Despite the suitability of this studied bioink, simulations have been performed with several simplifications, such as not-defined wall friction, the use of a bioink without cells inside, and no interaction between the bioink filament and the printing substrate. Additionally, only conical nozzle geometries have been simulated. As future works, a comparative study of how conical and needle tips geometries should deeply analyze the effect of shear stress under different temperatures of the bioink. Furthermore, other bioprinting settings, such as different height (h) or XY-plane speed, should be also included in future simulations to analyze the bioink filament in dynamic conditions during its deposition on the printing substrate. Finally, experimental tests using this commercial bioink with a 3D bioprinter should be performed to validate simulation results with the actual behavior of bioinks.

Author Contributions: Conceptualization, J.C.G.-B., A.D.-P. and J.B.P.; Formal analysis, J.C.G.-B.; Investigation, J.C.G.-B., E.M.-S. and J.B.P.; Methodology, J.C.G.-B. and E.M.-S.; Project administration, J.C.G.-B. and J.B.P.; Software, J.C.G.-B., E.M.-S., A.C.M. and M.M.; Supervision, J.B.P.; Writing—original draft, J.C.G.-B.; Writing—review and editing, J.C.G.-B., E.M.-S., A.C., M.M., A.D.-P. and J.B.P. All authors have read and agreed to the published version of the manuscript.

Funding: This research was co-financed by Consejería de Economía, Ciencia y Agenda Digital, Junta de Extremadura, project number IB16200 and predoctoral grant number PD16067 to J.C.G.-B. Co-financed by European Union/ERDF and ESF funds.

Conflicts of Interest: The authors declare no conflict of interest.

References

1. Ng, W.L.; Chua, C.K.; Shen, Y.F. Print Me An Organ! Why We Are Not There Yet. *Prog. Polym. Sci.* **2019**, *97*, 101145. [CrossRef]
2. Zhang, Y.S.; Yue, K.; Aleman, J.; Mollazadeh-Moghaddam, K.; Bakht, S.M.; Yang, J.; Jia, W.; Dell'Erba, V.; Assawes, P.; Shin, S.R.; et al. 3D Bioprinting for Tissue and Organ Fabrication. *Ann. Biomed. Eng.* **2016**, *45*, 148–163. [CrossRef] [PubMed]
3. Zhang, B.; Gao, L.; Ma, L.; Luo, Y.; Yang, H.; Cui, Z. 3D Bioprinting: A Novel Avenue for Manufacturing Tissues and Organs. *Engineering* **2019**, *5*, 777–794. [CrossRef]
4. Kyle, S.; Jessop, Z.M.; Al-Sabah, A.; Whitaker, I.S. 'Printability' of Candidate Biomaterials for Extrusion Based 3D Printing: State-of-the-Art. *Adv. Healthc. Mater.* **2017**, *6*. [CrossRef] [PubMed]
5. Rutz, A.L.; Gargus, E.S.; Hyland, K.E.; Lewis, P.L.; Setty, A.; Burghardt, W.R.; Shah, R.N. Employing PEG crosslinkers to optimize cell viability in gel phase bioinks and tailor post printing mechanical properties. *Acta Biomater.* **2019**, *99*, 121–132. [CrossRef]
6. Zhang, J.; Wehrle, E.; Vetsch, J.R.; Paul, G.R.; Rubert, M.; Müller, R. Alginate dependent changes of physical properties in 3D bioprinted cell-laden porous scaffolds affect cell viability and cell morphology. *Biomed. Mater.* **2019**, *14*, 065009. [CrossRef]

7. Chung, J.H.Y.; Naficy, S.; Yue, Z.; Kapsa, R.; Quigley, A.; Moulton, S.E.; Wallace, G.G. Bio-ink properties and printability for extrusion printing living cells. *Biomater. Sci.* **2013**, *1*, 763–773. [CrossRef]
8. Gao, T.; Gillispie, G.J.; Copus, J.S.; Kumar, A.P.R.; Seol, Y.-J.; Atala, A.; Yoo, J.J.; Lee, S.J. Optimization of gelatin-alginate composite bioink printability using rheological parameters: A systematic approach. *Biofabrication* **2018**, *10*. [CrossRef]
9. He, Y.; Yang, F.; Zhao, H.; Gao, Q.; Xia, B.; Fu, J. Research on the printability of hydrogels in 3D bioprinting. *Sci. Rep.* **2016**, *6*, 29977. [CrossRef]
10. Jeon, O.; Lee, Y.B.; Hinton, T.J.; Feinberg, A.W.; Alsberg, E. Cryopreserved cell-laden alginate microgel bioink for 3D bioprinting of living tissues. *Mater. Today Chem.* **2019**, *12*, 61–70. [CrossRef]
11. Pepelanova, I.; Kruppa, K.; Scheper, T.; Lavrentieva, A. Gelatin-methacryloyl (GelMA) hydrogels with defined degree of functionalization as a versatile toolkit for 3D cell culture and extrusion bioprinting. *Bioengineering* **2018**, *5*, 55. [CrossRef] [PubMed]
12. Raddatz, L.; Lavrentieva, A.; Pepelanova, I.; Bahnemann, J.; Geier, D.; Becker, T.; Scheper, T.; Beutel, S. Development and application of an additively manufactured calcium chloride nebulizer for alginate 3D-bioprinting purposes. *J. Funct. Biomater.* **2018**, *9*, 63. [CrossRef]
13. Wu, D.; Yu, Y.; Tan, J.; Huang, L.; Luo, B.; Lu, L.; Zhou, C. 3D bioprinting of gellan gum and poly (ethylene glycol) diacrylate based hydrogels to produce human-scale constructs with high-fidelity. *Mater. Des.* **2018**, *160*, 486–495. [CrossRef]
14. Zheng, Z.; Wu, J.; Liu, M.; Wang, H.; Li, C.; Rodriguez, M.J.; Li, G.; Wang, X.; Kaplan, D.L. 3D Bioprinting of Self-Standing Silk-Based Bioink. *Adv. Healthc. Mater.* **2018**, *7*, 1701026. [CrossRef]
15. Jia, J.; Richards, D.J.; Pollard, S.; Tan, Y.; Rodriguez, J.; Visconti, R.P.; Trusk, T.C.; Yost, M.J.; Yao, H.; Markwald, R.R.; et al. Engineering alginate as bioink for bioprinting. *Acta Biomater.* **2014**, *10*, 4323–4331. [CrossRef]
16. Kiyotake, E.A.; Douglas, A.W.; Thomas, E.E.; Detamore, M.S. Development and quantitative characterization of the precursor rheology of hyaluronic acid hydrogels for bioprinting. *Acta Biomater.* **2019**, *95*, 176–187. [CrossRef]
17. Ashammakhi, N.; Ahadian, S.; Xu, C.; Montazerian, H.; Ko, H.; Nasiri, R.; Barros, N.; Khademhosseini, A. Bioinks and bioprinting technologies to make heterogeneous and biomimetic tissue constructs. *Mater. Today Biol.* **2019**, *1*, 23. [CrossRef]
18. Donderwinkel, I.; van Hest, J.C.M.; Cameron, N.R. Bio-inks for 3D bioprinting: Recent advances and future prospects. *Polym. Chem.* **2017**, *8*, 4451–4471. [CrossRef]
19. Mancha-Sánchez, E.; Gómez-Blanco, J.C.; López-Nieto, E.; García-Casado, J.; Macías, A.; Díaz-Díez, M.A.; Carrasco-Amador, J.P.; Torrejón, D.; Sanchez-Margallo, F.M.; Pagador, J.B. Hydrogels for bioprinting: A systematic review of hydrogels synthesis, bioprinting parameters and bioprinted structures behavior. *Front. Bioeng. Biotechnol.* **2020**, in press. [CrossRef]
20. Ouyang, L.; Yao, R.; Zhao, Y.; Sun, W. Effect of bioink properties on printability and cell viability for 3D bioplotting of embryonic stem cells. *Biofabrication* **2016**, *8*, 1–12. [CrossRef]
21. Kim, W.J.; Kim, G.H. 3D bioprinting of functional cell-laden bioinks and its application for cell-alignment and maturation. *Appl. Mater. Today* **2020**, 19. [CrossRef]
22. Dutta, S.; Cohn, D. Temperature and pH responsive 3D printed scaffolds. *J. Mater. Chem. B* **2017**, *5*, 9514–9521. [CrossRef] [PubMed]
23. Axpe, E.; Oyen, M.L. Applications of alginate-based bioinks in 3D bioprinting. *Int. J. Mol. Sci.* **2016**, *17*, 1976. [CrossRef] [PubMed]
24. Zhou, D.; Chen, J.; Liu, B.; Zhang, X.; Li, X.; Xu, T. Bioinks for jet-based bioprinting. *Bioprinting* **2019**, 16. [CrossRef]
25. Zhang, S.; Vijayavenkataraman, S.; Lu, W.F.; Fuh, J.Y.H. A review on the use of computational methods to characterize, design, and optimize tissue engineering scaffolds, with a potential in 3D printing fabrication. *J. Biomed. Mater. Res. Part B Appl. Biomater.* **2019**, *107*, 1329–1351. [CrossRef]
26. Göhl, J.; Markstedt, K.; Mark, A.; Håkansson, K.; Gatenholm, P.; Edelvik, F. Simulations of 3D bioprinting: Predicting bioprintability of nanofibrillar inks. *Biofabrication* **2018**, *10*. [CrossRef]
27. Li, Y.; Verrelli, D.I.; Yang, W.; Qian, Y.; Chong, W. A pilot validation of CFD model results against PIV observations of haemodynamics in intracranial aneurysms treated with flow-diverting stents. *J. Biomech.* **2020**, *100*, 109590. [CrossRef]

28. Yan, K.C.; Paluch, K.; Nair, K.; Sun, W. Effects of process parameters on cell damage in a 3d cell printing process. In Proceedings of the ASME International Mechanical Engineering Congress and Exposition, Vancouver, BC, Canada, 12–18 November 2010; Volume 2, pp. 75–81.
29. Blaeser, A.; Duarte Campos, D.F.; Puster, U.; Richtering, W.; Stevens, M.M.; Fischer, H. Controlling Shear Stress in 3D Bioprinting is a Key Factor to Balance Printing Resolution and Stem Cell Integrity. *Adv. Healthc. Mater.* **2016**, *5*, 326–333. [CrossRef]
30. Liu, W.; Heinrich, M.A.; Zhou, Y.; Akpek, A.; Hu, N.; Liu, X.; Guan, X.; Zhong, Z.; Jin, X.; Khademhosseini, A.; et al. Extrusion Bioprinting of Shear-Thinning Gelatin Methacryloyl Bioinks. *Adv. Healthc. Mater.* **2017**, *6*, 1–11. [CrossRef]
31. Martanto, W.; Baisch, S.M.; Costner, E.A.; Prausnitz, M.R.; Smith, M.K. Fluid dynamics in conically tapered microneedles. *AIChE J.* **2005**, *51*, 1599–1607. [CrossRef]
32. Magalhães, I.P.; de Oliveira, P.M.; Dernowsek, J.; Las Casas, E.B.; Las Casas, M.S. Investigation of the effect of nozzle design on rheological bioprinting properties using computational fluid dynamics. *Rev. Mater.* **2019**, *24*. [CrossRef]
33. Reid, J.A.; Mollica, P.A.; Johnson, G.D.; Ogle, R.C.; Bruno, R.D.; Sachs, P.C. Accessible bioprinting: Adaptation of a low-cost 3D-printer for precise cell placement and stem cell differentiation. *Biofabrication* **2016**, *8*, 025017. [CrossRef] [PubMed]
34. Leppiniemi, J.; Lahtinen, P.; Paajanen, A.; Mahlberg, R.; Metsä-Kortelainen, S.; Pinomaa, T.; Pajari, H.; Vikholm-Lundin, I.; Pursula, P.; Hytönen, V.P. 3D-Printable Bioactivated Nanocellulose-Alginate Hydrogels. *ACS Appl. Mater. Interfaces* **2017**, *9*, 21959–21970. [CrossRef] [PubMed]
35. Nair, K.; Yan, K.C.; Sun, W. A computational modeling approach for the characterization of mechanical properties of 3D alginate tissue scaffolds. *J. Appl. Biomater. Biomech.* **2008**, *6*, 35–46. [CrossRef]
36. Smith, C.; Oldt, G. Multiaxial Bio-Printer Head. Available online: https://5f6357c8-abe2-426e-bc22-b9f609a0b347.filesusr.com/ugd/e69967_73cde5aebac44f11b0432814832a2110.pdf (accessed on 17 July 2020).
37. Li, M.; Tian, X.; Kozinski, J.A.; Chen, X.; Hwang, D.K. Modeling Mechanical Cell Damage In The Bioprinting Process Employing A Conical Needle. *J. Mech. Med. Biol.* **2015**, *15*, 1–15. [CrossRef]
38. Stewart, B. 3D Bioprinting Hydrogel for Tissue Engineering an Ascending Aortic Scaffold. Master's Thesis, University of Denve, Denver, CO, USA, June 2017.
39. Billiet, T.; Gevaert, E.; De Schryver, T.; Cornelissen, M.; Dubruel, P. The 3D printing of gelatin methacrylamide cell-laden tissue-engineered constructs with high cell viability. *Biomaterials* **2014**, *35*, 49–62. [CrossRef]
40. Liravi, F.; Darleux, R.; Toyserkani, E. Additive manufacturing of 3D structures with non-Newtonian highly viscous fluids: Finite element modeling and experimental validation. *Addit. Manuf.* **2017**, *13*, 113–123. [CrossRef]
41. Samanipour, R.; Wang, Z.; Ahmadi, A.; Kim, K. Experimental and computational study of microfluidic flow-focusing generation of gelatin methacrylate hydrogel droplets. *J. Appl. Polym. Sci.* **2016**, *133*, 24–26. [CrossRef]
42. Gretzinger, S.; Beckert, N.; Gleadall, A.; Lee-Thedieck, C.; Hubbuch, J. 3D bioprinting—Flow cytometry as analytical strategy for 3D cell structures. *Bioprinting* **2018**, *11*, e00023. [CrossRef]
43. Kesti, M.; Fisch, P.; Pensalfini, M.; Mazza, E.; Zenobi-Wong, M. Guidelines for standardization of bioprinting: A systematic study of process parameters and their effect on bioprinted structures. *BioNanoMaterials* **2016**, *17*, 193–204. [CrossRef]
44. Sultan, S.; Siqueira, G.; Zimmermann, T.; Mathew, A.P. 3D printing of nano-cellulosic biomaterials for medical applications. *Curr. Opin. Biomed. Eng.* **2017**, *2*, 29–34. [CrossRef]
45. Müller, M.; Öztürk, E.; Arlov, Ø.; Gatenholm, P.; Zenobi-Wong, M. Alginate Sulfate–Nanocellulose Bioinks for Cartilage Bioprinting Applications. *Ann. Biomed. Eng.* **2017**, *45*, 210–223. [CrossRef]
46. Cellink Bioink Biopritning Protocol. Available online: https://www.cellink.com/wp-content/uploads/2019/03/Bioprinting-Protocol-CELLINK-Bioink_21-Mars-2019.pdf (accessed on 17 July 2020).
47. COMSOL®. *CFD Module User's Guide*; COMSOL Inc.: Stockholm, Sweden, 2016; ISBN 1781273332.
48. Bartnikowski, M.; Wellard, R.M.; Woodruff, M.; Klein, T. Tailoring hydrogel viscoelasticity with physical and chemical crosslinking. *Polymers* **2015**, *7*, 2650–2669. [CrossRef]
49. Jalaal, M.; Cottrell, G.; Balmforth, N.; Stoeber, B. On the rheology of Pluronic F127 aqueous solutions. *J. Rheol. (NY)* **2017**, *61*, 139–146. [CrossRef]

50. Markstedt, K.; Mantas, A.; Tournier, I.; Martínez Ávila, H.; Hägg, D.; Gatenholm, P. 3D bioprinting human chondrocytes with nanocellulose-alginate bioink for cartilage tissue engineering applications. *Biomacromolecules* **2015**, *16*, 1489–1496. [CrossRef] [PubMed]
51. Lee, K.Y.; Mooney, D.J. Alginate: Properties and biomedical applications. *Prog. Polym. Sci.* **2013**, *37*, 106–126. [CrossRef]
52. Pati, F.; Jang, J.; Lee, J.W.; Cho, D.W. Extrusion bioprinting. In *Essentials of 3D Biofabrication and Translation*; Elsevier Inc.: Pohang-si, Korea, 2015; pp. 123–152. ISBN 9780128010150.